

基于焊丝深熔模式的铝/铜激光熔钎焊工艺研究

姜仁杰, 程智伟, 武强*, 肖荣诗

北京工业大学材料与制造学部智能光子制造研究中心, 北京 100124

摘要 采用基于焊丝深熔模式的熔钎焊方法,进行了 1060 铝合金和 T2 紫铜异种金属的激光填丝焊工艺研究。利用高速摄像机观测焊丝熔化的过渡行为,采用光学显微镜、X 射线衍射仪、扫描电镜、显微硬度仪及拉伸试验机对焊缝形貌、接头组织及性能进行表征。结果表明,采用不同的坡口形式和尺寸,使激光束在坡口中的作用位置偏向铜侧,这有利于焊缝成形。熔钎焊接头成形良好,无咬边缺陷。接头拉伸强度可达铝母材的 80%,接头断裂发生在界面层,断裂方式为脆性断裂。在焊缝界面层,存在笋状和胞状的铝/铜金属间化合物。XRD 检测结果表明,金属间化合物由 Al_2Cu 相和 Al_4Cu_9 相组成。界面层在铜侧钎焊区中部及下部分布均匀,厚度约为 20 μm 。

关键词 激光技术; 异种金属; 深熔模式; 填丝熔钎焊; 坡口形式; 组织性能

中图分类号 TG442

文献标志码 A

doi: 10.3788/CJL202148.2202013

1 引言

近年来,各类工程结构因为应用环境的多样性和制造成本的经济性需求,通常采用复合结构^[1-2]。纯铝和纯铜均具有优异的导电导热性能以及耐腐蚀性能,被广泛应用于航空航天、换热设备、电子产品及电池领域。铜和铝的密度及成本均具有较大差异,为了充分发挥两种材料的物性特点,降低构件成本,铝/铜复合结构应运而生,在工业领域内具有较大的应用需求。实现铝/铜可靠焊接是实现铝/铜复合结构可靠应用的关键所在。

近年来,熔钎焊方法受到国内外广泛关注。采用激光作为热源的熔钎焊技术,具有热源能量精确可控、光束变换灵活等优点,是熔点差异较大的异种金属的理想焊接方法之一^[3]。Solchenbach 等^[4]对铝箔和铜箔进行了激光熔钎焊研究,利用光纤激光器与二维电流扫描器,通过在焊接方向上叠加圆周运动,获取了均匀的金属间化合物层,Al 和 Cu 层界面的温度均匀分布,并接头最大抗剪强度可达 121 MPa。Jarwitz 等^[5]同样采用调制激光束对 1 mm 厚铝/铜薄板进行搭接焊,发现空间波束振荡

可以使焊接深度和宽度相互独立,进而获得较高的宽深比,这有助于降低接头的电阻。Lee 等^[6]在对铝/铜进行焊接时,发现不同的搭接配置对接头载荷和强度的影响不大,较高的焊接速度可有效抑制金属间化合物的生长。董鹏等^[7]对 3 mm 厚的铝合金和紫铜进行激光深熔钎焊,结果表明,界面层发现了 Al_2Cu_3 和 Al_2Cu 金属间化合物,且当铜母材熔化较少时,所获得的拉伸强度最高,为铝母材的 94%。Yan 等^[8]发现,在 Al/Cu 界面预置 Ni 箔夹层,可以减少界面处的金属间化合物,铝/铜异种金属搭接熔钎焊接接头的拉伸剪切强度得到增强。Mai 等^[9]发现,在铝/铜焊接试验中,减小脉冲激光的能量输入以及调整激光作用位置,可以减少脆性金属间化合物的生成,提高接头质量。Zhou 等^[10]在利用 Zn-15%Al 焊丝对 5052 铝合金和 H62 黄铜进行激光对接熔钎焊时,发现在较低焊速下可获得较好成形的接头,较高焊速时容易出现背部未熔透及裂纹缺陷,此时接头强度约为 Al 母材的 55.7%。Feng 等^[11]通过填充 $AlCu_5$ 焊丝,对 Al/Cu 进行了搭接熔钎焊,他们发现添加在焊丝中的 Cu 有助于提高焊丝熔滴在母材金属表面的浸润铺展性能,而控制热

收稿日期: 2021-05-13; 修回日期: 2021-05-30; 录用日期: 2021-06-15

基金项目: 国家自然科学基金面上项目(51775009)

通信作者: *jluwqiang@bjut.edu.cn

输入有助于减少金属间化合物的生成,接头强度约为 Al 母材的 75%。

传统的激光填丝焊方式都是将激光作用在母材上,利用熔池和激光对焊丝进行熔化,实现对接焊缝的熔钎焊。而对于异种材料而言,该工艺难以精确控制母材的熔化,板材的厚度也受到限制。为了满足铝/铜复合结构的制造需求,实现铝/铜异种材料的熔钎焊,本文在铝/铜对接位置处开坡口,使激光直接辐照焊丝,利用深熔模式实现焊丝的高速熔化^[12-13],并填充坡口,形成熔钎焊缝。通过研究坡口形貌和光丝作用点位置对焊缝成形的影响规律,获取了优化工艺参数及熔钎接头,并对焊缝的微观组织和性能进行了观察和分析。

2 试验方法及设备

试验采用 YLS-6000 光纤激光器,波长为

1060~1070 nm,额定输出功率为 6 kW,传输光纤芯径为 200 μm ,聚焦镜焦距为 200 mm。送丝机构为 WF-007A 多功能自动氩弧填丝机,运动系统为 KUKA 机械手。试验材料为 1060 铝合金和 T2 紫铜,尺寸为 100 mm \times 50 mm \times 3 mm,1060 铝合金焊前采用质量分数为 20% 的 NaOH 溶液去除表面氧化膜,并用体积分数为 30% 的 HNO₃ 溶液中和样件表面的残留碱液。T2 紫铜采用体积分数为 30% 的 H₂SO₄ 进行酸洗,清水冲洗酸液。化学清洗完成后,用砂纸将待焊部位打磨并用丙酮清洗油污。

试验原理图如图 1 所示,所设计的 4 种坡口的具体尺寸参数如表 1 所示,其中 W_1 和 W_2 为铜侧和铝侧底部的平面宽度, R_1 和 R_2 为铜侧和铝侧的过渡圆弧半径, θ_1 和 θ_2 为铜侧和铝侧的单边坡口角度, t 为钝边厚度, δ 为板材厚度。

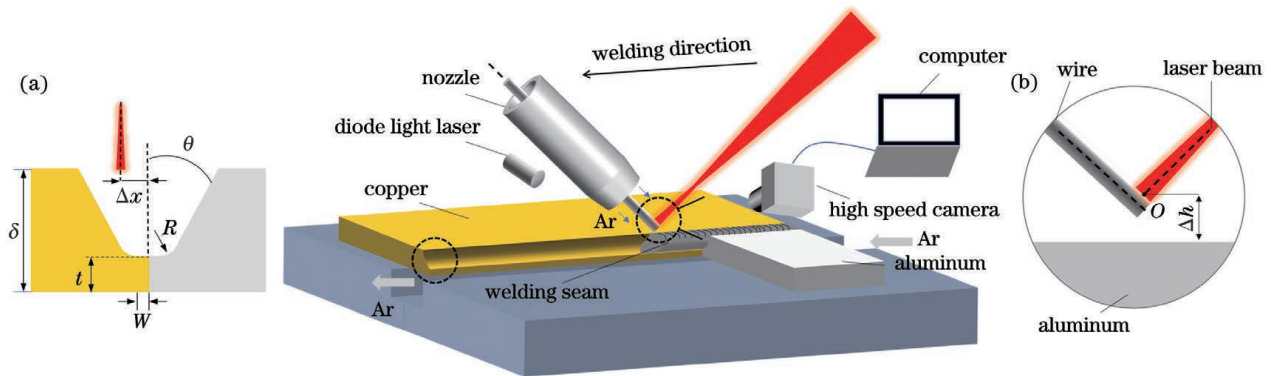


图 1 试验装置布置图。(a)坡口尺寸;(b)光丝作用点位置

Fig. 1 Layout of test device. (a) Groove size; (b) action point position between laser beam and wire

表 1 不同坡口的尺寸参数

Table 1 Specific size parameters of different grooves

Number	Groove at copper side				Groove at aluminum side			
	W_1/mm	t/mm	$\theta_1/(\text{^\circ})$	R_1/mm	W_2/mm	t/mm	$\theta_2/(\text{^\circ})$	R_2/mm
1#	0	0.8	5	0.6	0	0.8	5	0.6
2#	0	0.8	30	0.6	0.6	0.8	30	0.6
3#	0.3	0.8	30	0.6	0.3	0.8	30	0.6
4#	0.3	0.4	10	0.6	0	0.4	15	0.5

表 2 中列出了光丝作用点位置 $\Delta h = 0$ 时各坡口形式下焊接试验的工艺参数,其中 P 为激光功率, V_w 为送丝速度, V 为焊接速度, Δx 为光丝作用点偏离钝边对接中心线的距离,规定偏向铜侧为正,反之为负。焊丝与激光束分别置于工件法线两侧,激光束直接作用于焊丝前端,其中光丝作用点距离工件上表面高度定义为 Δh ,规定光丝作用点在母材

上表面以上为正,反之为负。

焊缝正面及背面采用氩气保护,气体流量均为 15 L/min。选用直径为 1.2 mm 的 ER4047 焊丝作为填充材料。在对焊丝熔化行为进行高速摄像观测时,采用单轴数控运动平台代替机械手完成焊接轨迹的运动。焊前将板材固定于活动平台上,利用计算机控制活动平台,改变焊接距离和速度。在观测

表 2 焊接参数

Table 2 Welding parameters

Number	Groove form	P /kW	$V_w/(m \cdot min^{-1})$	$V/(m \cdot min^{-1})$	Δx /mm
A-1	1#	4.5	5.0	1	0
A-2	1#	5.0	5.5	1	0
B-1	2#	5.0	5.5	1	-0.3
C-1	3#	5.0	5.5	1	0
D-1	4#	4.0	4.5	1	0.3
D-2	4#	4.5	5.5	1	0.3

过程中,将光丝作用点置于高速摄像机的视场内。

焊后针对各焊缝制备金相试样,进行粗磨和精抛后,使用 Keller 试剂(1 mL HF+1.5 mL HCL+2.5 mL HNO₃+95 mL H₂O)腐蚀 5~8 s。采用光学显微镜、扫描电子显微镜(SEM)及 X 射线衍射仪(XRD)对焊缝微观组织及物相组成进行表征。使用万能拉伸试验机对接头力学性能进行测试。使用

维式显微硬度仪对焊缝横截面进行硬度分析,两点之间的测试间隔为 0.1 mm,试样载荷为 0.98 N,加载时间为 15 s。

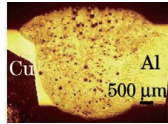
3 试验结果与分析

3.1 坡口尺寸对焊缝成形的影响规律

表 3 为表 2 中试样的焊缝成形和横截面图。

表 3 焊缝及焊缝横截面形貌

Table 3 Weld morphologies and weld cross-sectional morphologies

Number	Position	Weld morphology	Weld cross-sectional morphology
A-1	Top		
	Back		
A-2	Top		
	Back		
B-1	Top		
	Back		
C-1	Top		
	Back		
D-1	Top		
	Back		
D-2	Top		
	Back		

1#坡口下的 A-1 和 A-2 试样的焊缝正面成形较好,但背面成形不稳定,并出现了局部未熔透的区域;从焊缝横截面来看,A-1 试样的焊缝横截面积相对较小,并在铜侧熔合线附近有未熔合缺陷;两个焊缝中的气孔较多。2#坡口下的 B-1 试样焊缝完全熔透,正面成形略差,有咬边缺陷;焊缝背面完全熔透,但在铜侧母材处有咬边缺陷。3#坡口下的 C-1 试样的焊缝正面成形较好,在铜侧出现咬边,但相较于 B-1 试样,咬边缺陷有所改善;焊缝背面完全熔透。

4#坡口下的 D-1 和 D-2 试样,铜侧坡口面积增加,底部钝边厚度减小。在低热输入条件下,焊缝正面成形良好,光滑连续,焊缝背面完全熔透,成形稳定,无明显缺陷产生。

因此,选择合理的坡口形式有助于减少咬边、侧壁未熔合等焊接缺陷,提高焊缝成形质量。在焊接

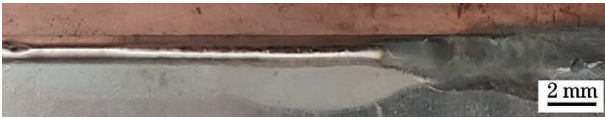
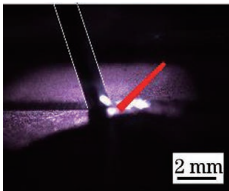
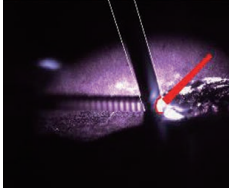
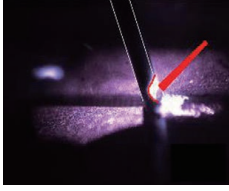
过程中,先利用激光束熔化焊丝,形成的液滴进入到母材坡口中,液滴持续吸收激光能量,铝母材熔化,形成熔池,熔池对铜侧母材进行浸润铺展,形成熔钎焊缝。通过优化坡口形状和尺寸,可改变激光在坡口内的作用位置(Δx)。当激光束偏铜侧时(4#坡口),激光能量在熔化焊丝的同时,也能透过焊丝施加于铜侧母材,具有更强的预热效果。铜侧坡口表面温度升高,导致液态金属在其表面的黏度降低,进而促进了焊丝熔滴及熔池在铜侧坡口表面的浸润和铺展,避免熔池在未充分填充坡口时发生凝固,进而造成咬边缺陷。

3.2 光丝作用点位置对焊缝成形的影响

当激光功率为 5000 W,送丝速度为 5.5 m/min,坡口形式为 2#时,不同 Δh 下的焊缝成形及高速摄像结果如表 4 所示。

表 4 Δh 对焊缝成形的影响

Table 4 Influences of Δh on weld formation

Δh /mm	Position	Weld morphology	High-speed camera image
-1	Top		
	Back		
0	Top		
	Back		
1	Top		
	Back		
2	Top		
	Back		

当 $\Delta h = -1$ mm 时,未形成有效焊缝。高速摄像结果表明,液滴没有将坡口填满,熔池较小。这可能是由于 Δh 过小,焊丝来不及完全熔化,顶丝造成激光束和焊丝的相对位置发生偏移,进而焊接过程中断。

当 $\Delta h = 0$ 时,焊缝正面成形连续均匀,焊缝背面完全熔透。根据高速摄像结果可知,此时熔滴过渡为液桥形式,并且在焊丝前端出现熔化前沿。Torkamany 等^[14]的研究表明,当足够高功率密度的激光束照射在焊丝上时,将会形成熔化前沿。此时焊丝以深熔模式吸收激光能量。

当 $\Delta h = 1$ mm 时,焊缝正面成形变差,铜侧坡口填充不饱满,焊缝宽度的一致性较差。高速摄像结果表明,此时焊丝前端熔化,前沿特征更加明显,具有熔滴过渡趋向。这与 Δh 的增加相关。一方面 Δh 值增加,表面张力对焊丝熔滴过渡的阻碍作用变大,导致液桥过渡不稳定。另一方面 Δh 值增加,导致激光在坡口内的作用位置与熔滴过渡位置的距离增大,加上铝/铜母材的能量热导率较高,预热效果不足,因此熔池浸润铺展能力下降,成形不稳定。

当 $\Delta h = 2$ mm 时,焊缝表面出现周期性瘤状液滴,焊缝背面完全没有熔透,此时高速摄像未观测到

焊丝前端出现熔化前沿。这可能是由于 Δh 值的进一步增加,焊丝虽然可以熔化,但是无法及时过渡到坡口中。随着焊丝熔滴不断积聚增大,液滴滴落到坡口中。

4 接头的显微组织分析

焊缝宏观形貌及铜侧焊缝不同位置处的显微组织如图 2 所示。接头可分为三个区域:铜侧钎焊区,焊缝中心区,铝侧熔化区。铝侧熔化区呈现铝合金激光焊接典型的熔化焊形貌,焊缝中间窄上下宽,这主要是由于上部和下部与空气接触,散热较慢,加上激光能量输入较高,而中部区域依靠母材散热较快,因此上部和下部熔化较多,中部熔化较少。

图 2(b)、(c)、(d)分别为 D-1 试样铜侧焊缝上部(区域 A)、中部(区域 B)和下部(区域 C)的显微组织,图 2(e)为焊缝中心区的显微组织。铜侧钎焊区可细分为三个区域:界面层,共晶区和焊缝区。焊缝中心区主要分布着灰白色网状结构。界面层上部区域形成了竹笋状金属间化合物,厚度约为 $50\ \mu\text{m}$ [图 2(b)],其生长方向垂直于熔合线方向。而界面层中部和下部胞状形态金属间化合物的厚度趋于均匀[图 2(c)、(d)],厚度约为 $20\ \mu\text{m}$ 。

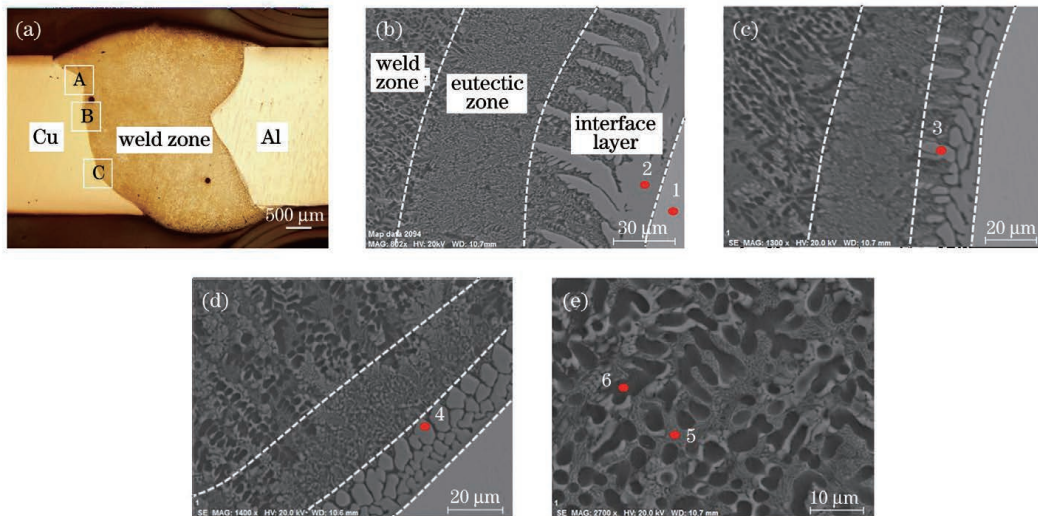


图 2 焊缝组织形貌。(a)焊缝横截面金相图;(b)界面层上部;(c)界面层中部;(d)界面层下部;(e)焊缝中心区
Fig. 2 Weld morphologies. (a) Metallographic diagram of weld cross section; (b) upper part of interface layer; (c) middle part of interface layer; (d) lower part of interface layer; (e) weld center area

上部和中下部的界面层厚度不均匀,分析其原因:此时 $\Delta h = 0$,光丝作用点位置位于坡口上表面,由于激光以深熔模式熔化焊丝,焊丝深熔时产生较高的热量,从而对坡口上部棱角处产生较强的加热效应,导致其熔化,并与熔池中的铝发生冶金结合,形成了较厚的 Al/Cu 金属间化合物。这也与焊缝

宏观形貌中的铜侧母材形貌相吻合。

图 3 为铜侧钎焊区下部的元素面扫描结果。可以看出,铜元素在界面层分布较多,在 Al/Cu 共晶区分布较少。铝元素在焊缝中心区和共晶区均分布较多,而在界面层分布较少。硅元素均匀分布在焊缝中心区和共晶区,界面层中分布较少。

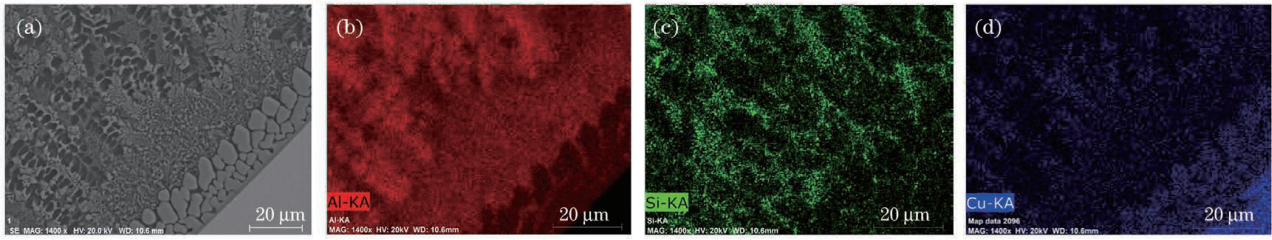


图 3 元素的面扫描结果。(a)界面层放大图;(b)Al 元素分布;(c)Si 元素分布;(d)Cu 元素分布

Fig. 3 Surface scan results of elements. (a) Magnified view of interface layer; (b) distribution of Al element; (c) distribution of Si element; (d) distribution of Cu element

表 5 所示为界面层和焊缝中心区的 EDS 测试结果。根据 Al-Cu 二元相图、Al-Si 二元相图以及元素相对原子比,可初步确定图 2(b)、(c)、(d)中点 2、3、4 处的组织为 Al_2Cu 金属间化合物,图 2(e)中点 5 的中灰白色网状结构组织为 $\alpha-Al$ 和 Al_2Cu 相,点 6 的黑色基体为 $\alpha-Al$ 和 Al-Si 共晶组织。在熔融焊丝填充下,熔池主要由 $\alpha-Al+Al-Si$ 共晶组织组成,由于铜侧母材上部棱角发生少量熔化,铜元素扩散进入熔池,随着熔池凝固,温度降低,发生共晶反应,生成了 $\alpha-Al$ 和 Al_2Cu ^[15]。

表 5 焊缝内的 EDS 结果
Table 5 EDS results in weld

Point No.	Atomic fraction of Cu / %	Atomic fraction of Al / %	Atomic fraction of Si / %
1	98.95	1.05	0
2	31.31	67.81	0.85
3	27.70	71.27	1.03
4	30.06	69.23	0.71
5	10.50	80.62	8.88
6	4.91	93.44	1.66

图 4 所示为焊缝横截面的 X 射线衍射分析结果。结果表明,界面层主要由 Al_2Cu 和 Al_4Cu_9 金属间化合物组成。根据吉布斯自由能大小可知,最

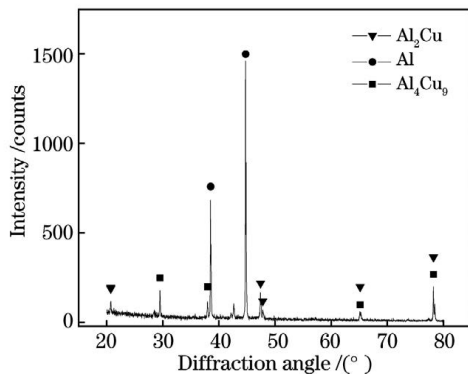


图 4 焊缝内 X 射线衍射分析图谱

Fig. 4 X-ray diffraction analysis pattern in weld

先生成的金属间化合物为 Al_2Cu ,其次是 Al_4Cu_9 ^[16]。随着铝元素和铜元素的不断溶解扩散,当浓度达到最大固溶度时,靠近铜侧的铜固溶体和铝固溶体生成了 Al_2Cu 。随着铜原子的继续扩散, Al_2Cu 在靠近铜侧界面处呈横向和纵向发展,形成了连续的 Al_2Cu 金属间化合物层。在进行 XRD 检测时,发现了 Al_4Cu_9 相衍射峰,这说明界面层生成了少量的 Al_4Cu_9 。

在 EDS 检测结果中,没有发现 Al_4Cu_9 ,这可能与 EDS 的检测范围和区域有关。在 Al_2Cu 逐渐扩展的基础上,Cu 原子和 Al 原子继续向对方方向扩散,当浓度达到一定浓度的时候,在 Al_2Cu 和固溶体 $\alpha-Al$ 界面处形成多个岛状或胞状的凸起,随着 Al 原子的浓度继续升高,生成了 Al_4Cu_9 ^[17-18]。

5 接头的力学性能

5.1 显微硬度

图 5 所示为 Al/Cu 接头的横截面显微硬度分布图。此时焊缝中心显微硬度较高。由于焊缝中心形成了 Al-Cu 和 Al-Si 共晶组织,因此其整体平均硬度要高于铝合金和纯铜母材。焊缝上部、中部和

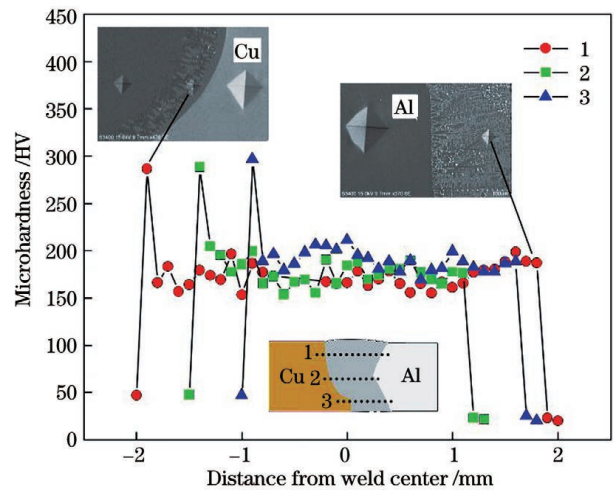


图 5 接头的显微硬度分布

Fig. 5 Microhardness distributions of joints

下部的硬度分布比较均匀,说明焊缝中心区形成的微观组织比较均匀。铜侧钎焊区界面层的硬度最高,达到 296 HV。这是因为在界面层分布着硬度较高的金属间化合物,界面层的硬度高于焊缝其他区域。

5.2 接头的强度与断口分析

图 6 为 D-1 和 D-2 试样熔钎焊接头的室温拉伸试验结果。去除接头余高后,接头的平均抗拉强度约为 80 MPa;未去除余高的接头拉伸强度约为 60 MPa,低于去除余高接头的拉伸强度。余高的去除减少了焊趾处产生的应力集中,提高了接头强度。

图 7 所示为拉伸断口的 SEM 图像。由图 7 可知,两种断口表面平整且存在撕裂棱,有典型的河流状花纹,为脆性断裂。不同断口区域处的元素组成

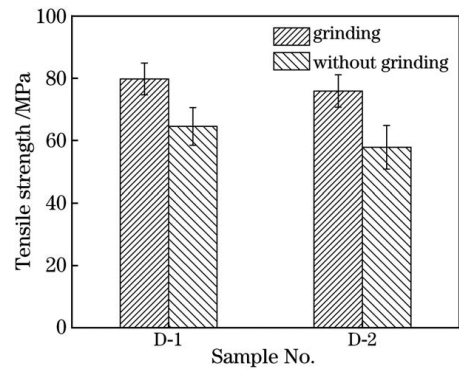


图 6 接头的抗拉强度

Fig. 6 Tensile strength of joints

如表 6 所示。根据 Al/Cu 元素的相对原子质量比,可推断断口处分布有 Al_2Cu 相,因此推测断裂发生在界面层。

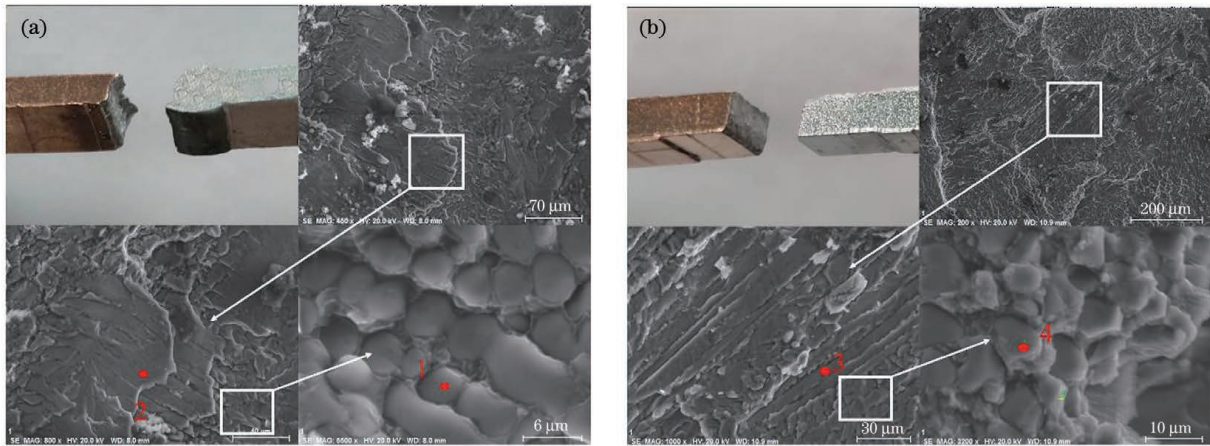


图 7 拉伸断口的 SEM 图像。(a)未去除余高;(b)去除余高后

Fig. 7 SEM images of tensile fractures. (a) Without grinding; (b) with grinding

表 6 接头断口区域的 EDS 结果

Table 6 EDS results of joint fracture areas

Point No.	Atomic fraction of Al / %	Atomic fraction of Cu / %	Atomic fraction of Si / %
1	64.38	33.66	1.96
2	65.10	34.54	3.36
3	65.81	31.86	2.33
4	83.66	18.37	2.03

6 结 论

采用基于焊丝深熔模式的铝/铜激光填丝熔钎焊方法获得了成形良好的接头,拉伸强度可达母材的 80%,断裂方式为脆性断裂,断裂发生在界面层。坡口形式和尺寸对焊缝成形及接头质量具有显著的影响。激光偏向铜侧,可以对铜基体产生较好的预

热效果,有利于熔池的浸润铺展,改善焊缝成形,抑制铜侧母材的咬边缺陷。铜侧钎焊区细分为三个区域:界面层、共晶区和焊缝区。上部界面层厚度约为 $50 \mu m$,中部和下部的界面层厚度约为 $20 \mu m$,界面层主要由 Al_2Cu 和 Al_4Cu_9 相组成。

参 考 文 献

[1] Wu X, Zhang P L, Tang M, et al. Formation and microstructure characteristics in spot welding of dissimilar Cu-Al foil by nanosecond laser scanning [J]. Chinese Journal of Lasers, 2019, 46 (4): 0402006.
吴希, 张培磊, 唐满, 等. 铜-铝异种箔片纳秒激光扫描点焊成形及组织特征 [J]. 中国激光, 2019, 46 (4): 0402006.

[2] Gu F, Sun Q, Huangpu Y X, et al. Effects of laser offset on microstructure and properties of NiTi/copper laser-welded joint [J]. Chinese Journal of

- Lasers, 2021, 48(10): 1002107.
- 顾凡, 孙茜, 皇甫圆翔, 等. 激光偏移量对镍钛/铜激光焊缝组织和性能的影响研究[J]. 中国激光, 2021, 48(10): 1002107.
- [3] Guo S, Peng Y, Zhu J, et al. Microstructure and mechanical properties of laser welded Ti/Al alloys [J]. Chinese Journal of Lasers, 2018, 45 (11): 1102010.
- 郭顺, 彭勇, 朱军, 等. 钛/铝激光焊接的微观组织及力学性能[J]. 中国激光, 2018, 45(11): 1102010.
- [4] Solchenbach T, Plapper P, Cai W. Electrical performance of laser braze-welded aluminum-copper interconnects[J]. Journal of Manufacturing Processes, 2014, 16(2): 183-189.
- [5] Jarwitz M, Fetzer F, Weber R, et al. Weld seam geometry and electrical resistance of laser-welded, aluminum-copper dissimilar joints produced with spatial beam oscillation [J]. Metals, 2018, 8 (7): 510-525.
- [6] Lee S J, Nakamura H, Kawahito Y, et al. Effect of welding speed on microstructural and mechanical properties of laser lap weld joints in dissimilar Al and Cu sheets [J]. Science and Technology of Welding and Joining, 2014, 19(2): 111-118.
- [7] Dong P, Chen K H, Xiao R S. Mechanical properties of aluminum-copper joint by laser penetration brazing [J]. Chinese Journal of Lasers, 2011, 38 (6): 0603009.
- 董鹏, 陈凯华, 肖荣诗. 铝-铜异种金属激光深熔钎焊接头力学性能 [J]. 中国激光, 2011, 38 (6): 0603009.
- [8] Yan S H, Shi Y. Influence of laser power on microstructure and mechanical property of laser-welded Al/Cu dissimilar lap joints [J]. Journal of Manufacturing Processes, 2019, 45: 312-321.
- [9] Mai T A, Spowage A C. Characterisation of dissimilar joints in laser welding of steel-kovar, copper-steel and copper-aluminium [J]. Materials Science and Engineering: A, 2004, 374(1/2): 224-233.
- [10] Zhou L, Luo L Y, Tan C W, et al. Effect of welding speed on microstructural evolution and mechanical properties of laser welded-brazed Al/brass dissimilar joints[J]. Optics & Laser Technology, 2018, 98: 234-246.
- [11] Feng J C, Liu Y B, Sun Q J, et al. Microstructures and properties of aluminum-copper lap-welded joints by cold metal transfer technology [J]. Advanced Engineering Materials, 2015, 17(10): 1480-1485.
- [12] Miranda R M, Lopes G, Quintino L, et al. Rapid prototyping with high power fiber lasers [J]. Materials & Design, 2008, 29(10): 2072-2075.
- [13] Xiao N. Research on new method of laser additive manufacturing based on deep penetration welding mode[D]. Beijing: Beijing University of Technology, 2018.
- 肖宁. 基于深熔焊模式的激光增材制造新方法研究 [D]. 北京: 北京工业大学, 2018.
- [14] Torkamany M J, Kaplan A F H, Ghaini F M, et al. Wire deposition by a laser-induced boiling front [J]. Optics & Laser Technology, 2015, 69: 104-112.
- [15] Li G, Song J F, Lu X F, et al. Investigation on microstructure and mechanical properties of Al/Cu butt joints by CMT method in asymmetrical V-groove configuration [J]. Metallurgical Research & Technology, 2020, 117(3): 303-314.
- [16] Liu Y B, Sun Q J, Wang H, et al. Effect of the axial external magnetic field on copper/aluminium arc weld joining [J]. Science and Technology of Welding and Joining, 2016, 21(6): 460-465.
- [17] Yuan X G, Lv L, Huang H J, et al. Effect of diffusion heat treatment on thickness of cold-rolled Cu/Al composite laminate interface [J]. Applied Mechanics and Materials, 2013, 310: 112-116.
- [18] Kah P, Vimalraj C, Martikainen J, et al. Factors influencing Al-Cu weld properties by intermetallic compound formation [J]. International Journal of Mechanical and Materials Engineering, 2015, 10(1): 1-13.

Research on Al/Cu Laser Brazing-Fusion Process Based on Wire Deep Penetration Mode

Jiang Renjie, Cheng Zhiwei, Wu Qiang*, Xiao Rongshi

High-Power and Ultrafast Laser Manufacturing Lab, Faculty of Materials and Manufacturing, Beijing University of Technology, Beijing 100124, China

Abstract

Objective Pure aluminum and pure copper have excellent electrical and thermal conductivities and corrosion resistance, and are widely used in aerospace, heat exchange equipment, electronic products and batteries. The density and cost of copper and aluminum are quite different. In order to give full play to the physical characteristics of these two materials and reduce the cost of components, the aluminum/copper composite structure has emerged as a great application requirement in the industrial field. How to achieve reliable welding of aluminum and copper is the key to the reliable application of aluminum and copper composite structures. This paper proposes a new method for laser brazing-fusion process based on the wire deep penetration mode, and conducts the welding process test and the analysis of the joint structure and performance.

Methods Laser wire filler brazing-fusion was performed for 3 mm thick aluminum/copper dissimilar metals, and the influences of groove size, process parameters and the height of the intersection of laser beam and wire from the base material were studied. Cleaning and mechanical grinding are needed to remove the oxide film before welding. Before welding, the 1060 aluminum alloy was first cleaned with the 20% (mass fraction) NaOH solution at 50–60 °C for 5 min to remove the surface oxide film. Then it was soaked in the 30% (volume fraction) HNO₃ solution for 5 min to neutralize the residual alkali. Finally, the aluminum alloy surface was rinsed with clean water, dried with compressed air, and stored in a sealed bag to avoid contact with air. T2 copper was pickled with the 30% (volume fraction) H₂SO₄ solution for 5 min, and the surface was washed with clean water to ensure that there was no acid residue on the surface. It was dried with compressed air and stored in a sealed bag. After chemical cleaning, the welding test shall be conducted within 12 h, otherwise the chemical cleaning of oxide film shall be conducted again. The aluminum alloy and pure copper plates with preset groove shall be assembled according to the zero gap butt joint method, horizontally placed on the surface of the worktable, and fixed with clamping tooling, so as to ensure that the assembly gap does not change during welding. High speed camera was used to observe and record the welding process. The high-speed camera was positioned at the welding pool, and the auxiliary light source was placed on the other side to irradiate the welding wire and pool. The CCD imaging system of the camera was used to transmit the image signal to the connected computer for real-time observation and recording. After the welding was completed, metallographic sample was prepared, and the sample was ground and polished. Then, the microstructure of the weld was observed with optical microscope and scanning electron microscope, and the joint performance was tested with universal tensile testing machine and microhardness tester.

Results and Discussions Choosing a reasonable groove form can help reduce welding defects such as undercuts and sidewalls that are not fused, and improve the quality of weld formation. The shape and size of the groove are optimized, and the position of the laser in the groove is changed. When the laser beam is biased to the copper side, the laser energy will melt the welding wire and at the same time act on the copper side base material, which has a stronger preheating effect (Table 3). When the height of the intersection of laser beam and wire from the base material is 0, the top view of the weld is continuous and uniform, and the back view of the weld is completely penetrated. According to the observation of high-speed camera, the droplet transition is in the form of liquid bridge. And there is a boiling front in the front of the welding wire. This shows that when the laser beam with an enough high power density irradiates on the welding wire, the melting front will be formed. At this time, the welding wire absorbs the laser energy in a deep penetration mode (Table 4). Scanning electron microscope observation results show that the joint can be divided into aluminum side melting zone, weld zone, and copper side brazing zone. The brazing area at the copper side can be finely divided into the interface layer, the eutectic zone, and the weld zone (Fig. 2). The interface layer is mainly composed of Al₂Cu intermetallic compounds, and a few Al₃Cu₉ phases are also generated (Fig. 4). The hardness distribution in the center of the weld is uniform, and the hardness of the interface

layer is up to 296 HV (Fig. 5). The average tensile strength of the joint with grinding is about 80 MPa. In contrast, the tensile strength of the joint without grinding is about 60 MPa (Fig. 6). The fracture surfaces of the two kinds of fractures are flat with tearing edges and typical river-like patterns, which can be judged as brittle fractures (Fig. 7).

Conclusions The aluminum/copper laser brazing-fusion process based on the wire deep penetration mode was used to obtain a well-formed joint, the tensile strength can reach 80% of that of the aluminum base metal, the fracture of the joint occurs in the interface layer which can be judged as brittle fractures. The groove form and size have significant influence on the weld formation and joint quality. When the laser is biased to the copper side, it can produce a better preheating effect on the copper matrix, which is conducive to the infiltration and spreading of the weld pool, improve the weld forming, and inhibit the undercut defect of the base metal on the copper side. The brazing area on the copper side is subdivided into three areas: the interface layer, the eutectic area, and the weld area. The thickness of the upper interface layer is about 50 μm , and the thicknesses of the middle and lower interface layers are about 20 μm . The interface layer is mainly composed of Al_2Cu and Al_4Cu_9 phases.

Key words laser technology; dissimilar metals; deep penetration modes; filler wire brazing-fusion; groove form; microstructures and properties

OCIS codes 140.3390; 160.3900; 140.3460